3-2014

REPAD: An empirical model of pitch angle distributions for energetic electrons in the Earth's outer radiation belt

Yue Chen
Los Alamos National Laboratory

R. Friedel
Los Alamos National Laboratory

M. G. Henderson
Los Alamos National Laboratory

S. Claudepierre
Aerospace Corporation

S. K. Morley
Los Alamos National Laboratory

See next page for additional authors

Recommended Citation

Chen, Y., R. H. W. Friedel, M. G. Henderson,S. G. Claudepierre, S. K. Morley, andH. Spence (2014), REPAD: An empiricalmodel of pitch angle distributions forenergetic electrons in the Earth'souterradiation belt, J. Geophys. Res. SpacePhysics, 119,1693–1708, doi: 10.100 2/2013JA019431.

AGU PUBLICATIONS

JGR

Journal of Geophysical Research: Space Physics

RESEARCH ARTICLE
10.1002/2013JA019431

Key Points:
- An empirical model for pitch-angle distributions of outer-belt e- from data
- Model is validated and evaluated, using RBSP data, and can be applied to GPS
- The e- PADs are highly stable for L ~4-5 but not outward (e.g, GEO with L~6.5)

Supporting Information:
- Readme
- Figure S1a
- Figure S1b
- Figure S2a
- Figure S2b
- Figure S3
- Figure S4
- Figure S5
- Figure S6
- Figure S7
- Figure S8a
- Figure S8b
- Figure S9
- Figure S10
- Text S1

Correspondence to:
Y. Chen,
cheny@lanl.gov

Citation:
Chen, Y., R. H. W. Friedel, M. G. Henderson, S. G. Claudepierre, S. K. Morley, and H. Spence (2014), REPAD: An empirical model of pitch angle distributions for energetic electrons in the Earth's outer radiation belt, *J. Geophys. Res. Space Physics*, *119*, 1693–1708, doi:10.1002/2013JA019431.

Received 9 SEP 2013
Accepted 25 JAN 2014
Accepted article online 31 JAN 2014
Published online 7 MAR 2014

REPAD: An empirical model of pitch angle distributions for energetic electrons in the Earth's outer radiation belt

Yue Chen[1], Reiner H. W. Friedel[1], Michael G. Henderson[1], Seth G. Claudepierre[2], Steven K. Morley[1], and Harlan E. Spence[3]

[1]Los Alamos National Laboratory, Los Alamos, New Mexico, USA, [2]The Aerospace Corporation, Los Angeles, California, USA, [3]University of New Hampshire, Durham, New Hampshire, USA

Abstract We have recently conducted a statistical survey on pitch angle distributions of energetic electrons trapped in the Earth's outer radiation belt, and a new empirical model was developed based upon survey results. This model—relativistic electron pitch angle distribution (REPAD)—aims to present statistical pictures of electron equatorial pitch angle distributions, instead of the absolute flux levels, as a function of energy, L shell, magnetic local time, and magnetic activity. To quantify and facilitate this statistical survey, we use Legendre polynomials to fit long-term in situ directional fluxes observed near the magnetic equator from three missions: CRRES, Polar, and LANL-97A. As the first of this kind of model, REPAD covers the whole outer belt region, providing not only the mean and median pitch angle distributions in the area but also error estimates of the average distributions. Preliminary verification and validation results demonstrate the reliable performance of this model. Usage of REPAD is mainly to predict the full pitch angle distribution of fluxes along a given magnetic field line, or even on a given drift shell, based upon one single unidirectional or omnidirectional flux measurement anywhere on that field line. This can be particularly useful for data assimilation, which usually has large tolerance on data errors. In addition, relatively small variations in pitch angle distributions measured at L shell between ~4 and 5 justify the assumption of fixed pitch angle distributions at GPS equatorial crossings (L ~ 4.2) used in our previous studies.

1. Introduction

Studying the pitch angle distribution (PAD) of trapped radiation belt particles has attracted intensive interests since the early days of magnetosphere research. This is mainly driven by the academic curiosity of understanding the cause of observed and varying PADs, which are often related to processes governing the dynamics of radiation belts. For example, energetic electrons (~MeV) observed at geosynchronous orbit experience strong enhancements after some geomagnetic storms but significant losses after others [*Reeves et al.*, 2003; *Chen et al.*, 2007b]. This should reflect the competition between various processes in each individual event, and tracking distributions and variations of electron PADs may help identify and evaluate those processes.

Meanwhile, practical needs also demand knowledge on electron PADs. For example, although the most efficient way to monitor radiation belts is to make fully directional measurements close to the magnetic equator, satellite orbits are often not so ideal due to other considerations and particle instruments on board may only measure electrons in either a single direction or omnidirection, such as GPS satellites in the latter case. Therefore, to maximize the usage of observations with limited resolution on pitch angles, it will be really useful to know not only the statistically averaged PAD but also its reliability. This work addresses this issue by developing a new PAD empirical model.

There exist several typical PAD types for electrons. The simplest one is the isotropic distribution, which is often observed in newly injected substorm electrons in the midnight sector at geosynchronous (GEO) orbit [*Åsnes et al.*, 2005]. Other well-known PADs include the pancake distribution, with a peak flux at 90° pitch angle, and the butterfly distribution, with a local minimum at 90° and a maximum before reaching each loss cone. The latter is also referred to as a cigar distribution sometimes. For relativistic electrons observed at GEO, pancake PADs generally dominate the dayside, while butterfly the nightside [*West et al.*, 1973; *Baker et al.*, 1978], and this difference is mostly due to the drift-shell splitting of electrons in a nonsymmetric magnetic

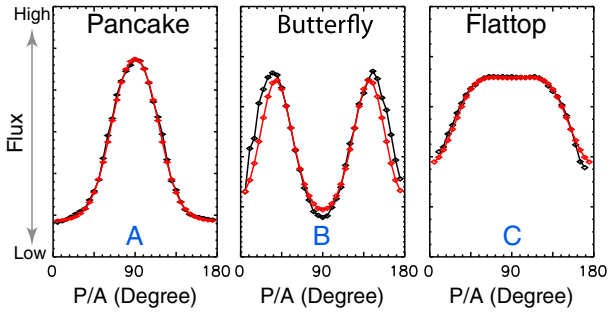

Figure 1. Three typical pitch angle distributions for radiation belt electrons. (a) Pancake distribution, (b) butterfly distribution, and (c) flattop distribution. Black dots (curves) are observed data, and red points (curves) are fitting results using Legendre polynomials as described in section 3.

field [*Roederer*, 1970]. Another common PAD is the flattop distribution, characterized by a near-flat distribution over a broad range of pitch angles centered at 90°. A previous study by *Horne et al.* [2003] has argued that the flattop PAD is the signature of in situ acceleration caused by wave-particle resonance, which can be differentiated from the pancake distribution resulting from inward radial diffusion. One example for each typical PAD is shown in Figure 1.

Electron PADs are not a new research topic. For instance, empirical radiation belt models, such as AE-8, provide average flux levels for the whole radiation belt region, which may implicitly provide PADs. However, since data samples used for the model are neither distributed evenly along each magnetic field line nor acquired simultaneously, the derived PADs are inevitably biased to some unknown degree. In an attempt to update outer zone energetic electron environment, *Vampola* [1998] conducted a statistical survey on CRRES electron data and presented the pitch angle distribution coefficient as a function of L shell, with the exclusion of butterfly distributions due to the form of selected fitting function. In addition, there are also other case and statistic studies directly focusing on electron PADs [e.g., *Horne et al.*, 2003; *Gannon et al.*, 2007; *Gu et al.*, 2011] that establish connections between variations in electron PADs and factors such as wave activities and storm events. Although revealing interesting physics, results from those studies are very useful for interpreting pitch angle resolved observations but not for non–pitch angle resolved observations.

In this report, we present a new empirical model for outer belt electrons. Based upon a statistical survey on electron observations accumulated during the last two decades, this relativistic electron pitch angle distribution (REPAD) model provides reliable PADs with error bars for energetic electrons along field lines trapped within L shells between three and nine. In addition, we reintroduce an effective PAD-fitting method that will be a very useful tool for future mining through large volume of pitch angle resolved data, such as data from the Van Allen Probes mission.

Descriptions on instruments, data, and preprocessing are given in section 2. Section 3 describes the fitting scheme, its efficiency, and presents model parameters. Some model results are presented in section 4, and section 5 shows model verification, validation, and evaluation results. Section 6 discusses the sample application to GPS data, and this report is concluded by a summary in section 7.

2. Instruments and Data

Long-term electron observations used here are from the Combined Release and Radiation Effects Satellite (CRRES, operating 1990–1991), Global Geospace Science Polar Satellite (Polar, 1996–2008), and one Los Alamos National Laboratory geosynchronous satellite LANL-97A (1999–2008). These three satellites have very different orbit configurations as described below, and the whole data set expands over ~22 satellite years in total.

CRRES was launched in July 1990 into a low-inclination (~18°) geosynchronous transfer orbit (GTO) until the mission was unexpectedly ended due to the loss of communication in October 1991. With the fluxgate magnetometer instrument aboard measuring local magnetic field [*Singer et al.*, 1992], the Medium Electrons A (MEA) [*Vampola*, 1992] spectrometer on CRRES provides pitch angle resolved electron data covering the energy range from 0.15 up to 1.7 MeV in 17 differential channels. MEA data used here have a time resolution of 1 min. The advantage of CRRES mission is its GTO which has good coverage of both L shells and the full PADs, and the disadvantage is the short mission period and the lack of data in the prenoon sector. Figure 2a presents one MEA data example, showing pitch angle resolved fluxes for 148 keV electrons on 1 day. Butterfly distributions observed at ~0100 UT and pancake distributions at ~0730 UT correspond to ~2200 and 1600 MLT (not shown), respectively, in the outer belt. Due to its high data quality, we will often use MEA data as examples later on.

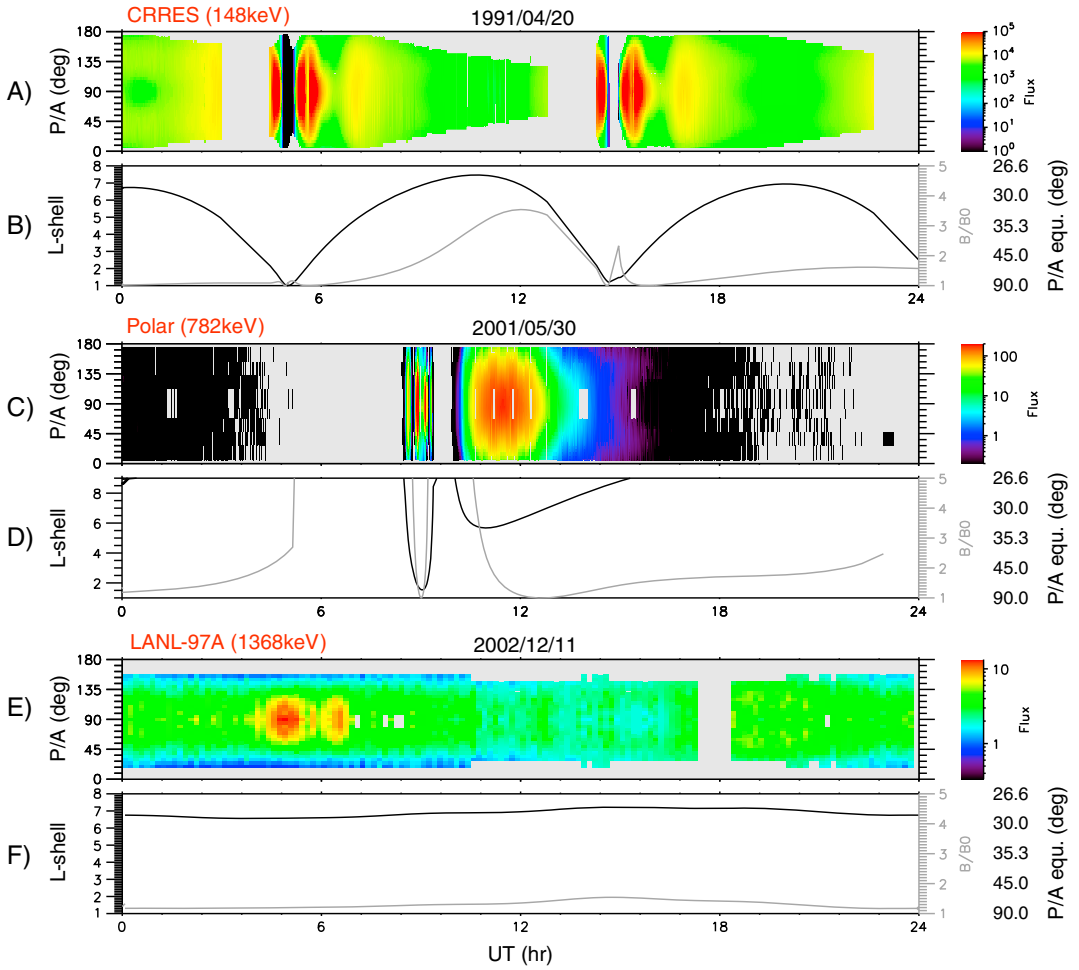

Figure 2. Data samples from three satellite missions. (a) Time series of pitch angle resolved fluxes for 148 keV electrons observed by CRRES on 1 day (20 April 1991) and (b) the corresponding L shell curve (black) and the ratio curve (gray) between local and equatorial magnetic field. Equatorial pitch angle values (black) corresponding to five magnetic ratios are also given to the right of the panel. (c and d) Polar fluxes for 782 keV electrons, L shells, and magnetic field ratios on 30 May 2001. (e and f) LANL-97A fluxes for 1368 keV electrons, L shells, and magnetic field ratios on 11 December 2002. Gray gaps in fluxes are due to the lack of measurements.

The Polar satellite has a high-inclination (~86°) polar orbit of 2 × 9 R_E, and the mission started in February 1996 and ended April 2008. Polar crosses the magnetic equatorial plane every ~9 h. Due to orbital precession, Polar's equatorial crossing keeps changing its radial distance with time slowly (e.g., it was around L ~ 4 in 1996 and L ~ 9 in 2002) and sweeps across all magnetic local times (MLTs) every ~12 months. This orbit configuration for Polar has the best spatial coverage among all three missions. With the Magnetic Field Experiment [*Russell et al.*, 1995] measuring local magnetic field, the comprehensive energetic particle and pitch angle distribution (CEPPAD) experiment [*Blake et al.*, 1995] onboard Polar provides pitch angle resolved flux data of energetic electrons, covering the energy range from 30 keV up to 10 MeV with detectors of the Imaging Electron Sensor and the High Sensitivity Telescope subsystems. Flux data used here have an average time resolution of 24 s. Only data with L > 3 are used to avoid potential contamination from protons [*Friedel et al.*, 2005]. Figure 2c presents one CEPPAD data example, showing pitch angle resolved fluxes for 782 keV electrons on 1 day. Pancake distributions between ~1030 and 1400 UT correspond to ~0900 MLT (not shown here) in the outer belt.

LANL-97A measures electrons in geosynchronous (GEO) orbit with a ~10° of magnetic latitude, and data used here range from 1999 to the beginning of 2008. The Synchronous Orbit Particle Analysis (SOPA) instrument [*Belian et al.*, 1992] measures directional electron distributions from 50 keV to 1.5 MeV. With no magnetic instrument aboard, the local magnetic field direction is indirectly derived from the symmetries of the plasma distribution [*Thomsen et al.*, 1996; also see *Chen et al.*, 2005, Appendix A]. Extra care has been taken to remove

contaminations from background and other possible sources by fitting measurements with two-Maxwellian distributions [*Cayton et al.*, 1989]. Flux data here have a time resolution of 10 min. Figure 2e presents one SOPA data example, showing pitch angle resolved fluxes for 1368 keV electrons on 1 day. Daily variations in PADs can be clearly seen with significant pancake PADs around local noon at ~0600 UT.

For all three data sets, the quiet Olson and Pfitzer magnetic field model [*Olson and Pfitzer*, 1977] together with the International Geomagnetic Reference Field (IGRF) are used for calculating the McIlwain's L shell [*McIlwain*, 1966], MLT values, and mapping local PADs down to the magnetic equator. We choose to use McIlwain's L instead of Roederer L* just for the reason of simplicity and convenience (see supporting information for more discussion). For developing REPAD, we select only local PADs measured within ± 15° magnetic latitude. This is a reasonable range picked after testing several values: Larger magnetic latitude ranges will leave the unmeasured pitch angle gap in the equatorial PAD too wide that we will not be able to capture some interesting features around the 90° pitch angle, and unreliable extrapolation is also unavoidable; smaller magnetic latitude ranges will discard many observations and make sample sizes too small to make the statistical sense. Intercalibration between instruments and data flagging have been performed in previous work [*Friedel et al.*, 2005] and applied here. For model development, CEEPAD and SOPA fluxes are all first interpolated to MEA's energy channels.

3. Pitch Angle Fitting Scheme and Model Formalism

One prerequisite for developing an empirical PAD model is an effective fitting method to quantify various PADs using limited parameters. Some previous studies have used the function form of $\sin^n(\alpha)$, where α is the pitch angle and n is the fitting parameter. This fitting function is good for presenting monotonically increasing and decreasing PADs between 0° and 90° pitch angles, as shown in previous studies [e.g., *Vampola*, 1998; *Gannon et al.*, 2007], but obviously has difficulty in fitting some PADs, such as butterfly distributions. This means that one parameter is not enough for this work and what we need is a full set of orthogonal functions. If we use the full set of trigonometric functions, however, the problem is that we may end up with too many fitting coefficients that are difficult to handle and interpret.

Since a PAD is indeed the distribution over a sphere with the inclusion of azimuthal angles, using the spherical harmonics is an appealing solution, and we thus select Legendre polynomials as the fitting function set. Here we focus on explaining the fitting scheme, and details about these polynomials $P_n[\cos(\alpha)]$ can be found in the supporting information.

$$\lg[j(\alpha)] = \sum_{n=0}^{\infty} C_n P_n[\cos(\alpha)] = |C_0| \sum_{n=0}^{\infty} c_n P_n[\cos(\alpha)] \tag{1}$$

As shown in equation (1), for a given pitch angle distribution $j(\alpha)$, we choose to fit to the logarithm of fluxes j for two reasons: First is to reduce the absolute variation range of PADs and the second is to avoid fitted flux values being unphysically negative later. The orthogonal relationship between polynomials enables us to calculate fitting coefficients C_n(c in upper case), and then we derive the normalized coefficients c_n (c in lower case),

$$c_n = \frac{C_n}{|C_0|} = \frac{(2n+1)\int_0^{\pi} \lg[j(\alpha)]^* P_n[\cos(\alpha)]^* \sin(\alpha) d\alpha}{\left|\int_0^{\pi} \lg[j(\alpha)]^* \sin(\alpha) d\alpha\right|} \tag{2}$$

as defined in equation (2). Since $|C_0|$ means the directionally average flux level for a distribution, coefficients c_n reflect the relative variations over the average level.

To help understanding the advantages of this fitting scheme, Figure 3 (top) plots several polynomials. First, trapped electrons request symmetric PADs over 90° pitch angle, which can be easily identified by coefficient values for the odd-th orders of P_n, and thus, all fittings with large values in c_1, c_3, etc. are questionable and consequently excluded from model samples. Second, shapes of P_2 (red) and P_4 (blue) are alike the typical pancake and butterfly PADs, upside down though, suggesting the values of the first several even-th orders of P_n may dominate others. This has been demonstrated by fitting observations throughout the CRRES mission, as one example in Figure 3 (bottom), and showing that c_n quickly decreases with increasing n. Therefore, this justifies to keep c_2, c_4, and c_6 being the only three fitting coefficients for REPAD. In fact, our discussions next will often only include c_2 and c_4 due to their much larger values. Finally, since the high even-th orders of P_n involves high-frequency fluctuations, e.g., the P_{20} curve (dashed black line) shown in Figure 3 (top), large values in the corresponding coefficients can be used for ruling out observations with poor statistics, which occur

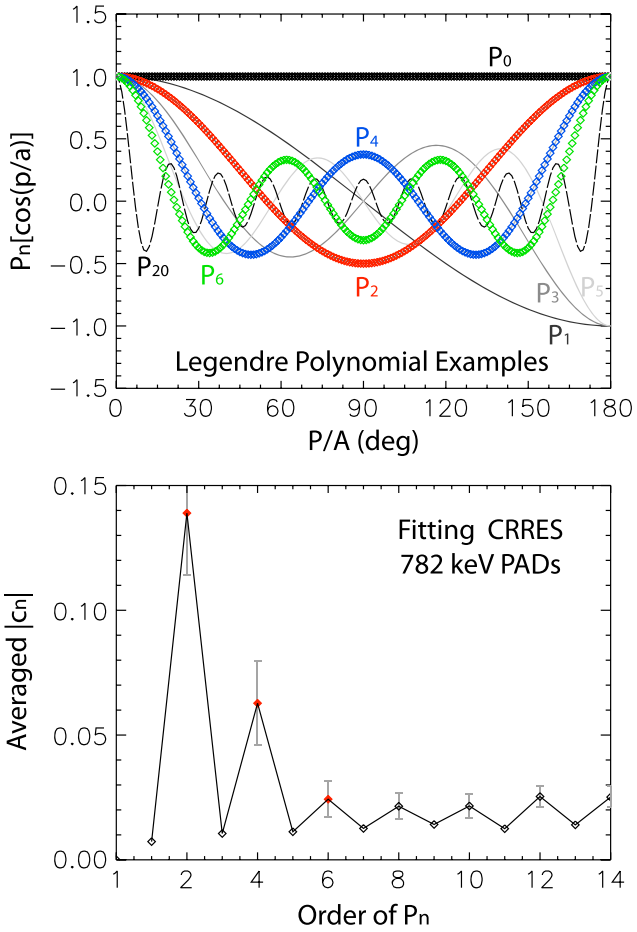

Figure 3. Legendre polynomial curves and average fitting coefficients. (top) Example curves for several Legendre polynomials as a function of pitch angles. (bottom) Average of absolute normalized fitting coefficients from $|c_1|$ to $|c_{14}|$, derived from fitting to 782 keV electron PADs measured during the whole CRRES mission. The standard deviations (gray bars) for all even-th order of $|c_n|$ are also plotted, and standard deviations for all odd-th order of $|c_n|$ are all <0.01 and not plotted here. Only coefficients for the first three even-th order of P_n (the three red data points) are kept for REPAD and the rest are ignored.

often for high-energy electrons. Therefore, advantages of Legendre polynomials make them appropriate for fitting particle PADs, particularly in automated processing of large volume of data. In addition, this is also an effective and efficient fitting scheme. For example, through the whole CRRES mission, there are ~98% (72%) observations for electrons with the lowest energy 148 keV (highest energy, 1582 keV) that can be fitted to a fairly high degree with the only three fitting coefficients. This helps rule out the possibility of data-preselecting bias introduced by the fitting scheme. Figure 1 already shows several fitting results, and extra examples for good and poor fitting can be found in Figure S1 in the supporting information that are randomly selected from fitting MEA data. Data with poor fitting are excluded from REPAD.

Values of coefficients c_n can be directly read for categorizing PAD types, and such examples are shown in Figure 4 that plots PADs corresponding to pairs of (c_2, c_4). Pancake PADs usually have negative c_2 and smaller values of $|c_4|$, such as those in Figure 4e; flattop PADs have both negative and comparable c_2 and c_4 values, such as those gray and green curves in Figure 4f; butterfly PADs have negative and large c_4 and smaller/comparable values of $|c_2|$, such as those in Figures 4g and 4h. In other words, by knowing the values of (c_2, c_4), one may immediately know the type of PADs. This is also significant for automated processing, e.g., picking out PADs with some specific types from large volume of data sets and thus facilitates identifying statistical relation between some PAD shape and other physics parameters such as geomagnetic activity indices.

It must be mentioned that using Legendre polynomials for fitting PADs is not a new idea. This method first appeared in the work by *Higbie and Moomey* [1977] and was later applied for analyzing GEO electron data in case studies [e.g., *Baker et al.*, 1978]. However, it is this work that for the first time thoroughly checks the method's effectiveness and further applies it to the development of a statistical model.

Now we explain the formalism of REPAD. For trapped radiation belt electrons, owning to Liouville's theorem, an off-equatorial PAD can always be magnetically converted to part of the equatorial PAD. Therefore, the spatial domain of REPAD is confined to the 2-D magnetic equator divided by many spatial bins with unequaled size. The center of each bin has the coordinates of (L, MLT), i.e., the McIlwain L shell and magnetic local time, as plotted in gray contours in Figure 5a. In addition, eight energy points, ranging from 148 up to 1582 keV, are used as the dimension to reflect energy dependence. Meanwhile, to reflect the PAD's dependence on magnetic activities, the model is further sorted into three *AE* categories. (Note that our selection of *AE* is simply based on the consideration of electron's cyclotron resonance with waves. There are other parameter options such as the *Dst* index, a representative of the changing global magnetic

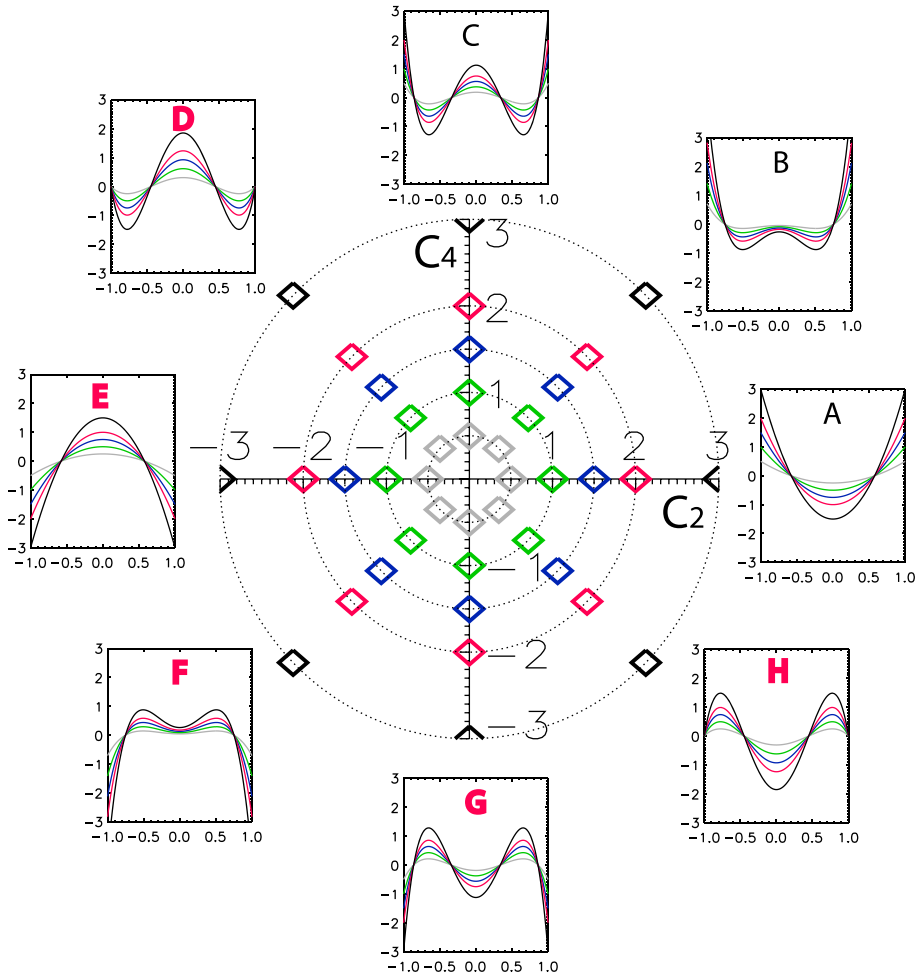

Figure 4. Shapes of PADs corresponding to selected (c_2, c_4) combinations. The central plot shows selected (c_2, c_4) pairs in various colors and magnitudes. For pairs in each radial direction, the corresponding PAD curves are plotted as a function of cos(α) in the same color in a small panel, distributed along the outermost circle along the same radial direction. All other fitting coefficients are assumed zero except for C_0 being one here. For example, pairs along the negative horizontal axis have PAD curves as shown in Figure 4e. (d–h) Panels marked with the bold red fonts are what typically observed in data, and (a–c) all others are much less commonly observed.

configuration that affects electron PADs. Here we leave this topic for future studies.) As mentioned above, we only keep three fitting coefficients, c_2, c_4, and c_6, for PAD shapes. Finally, in each model bin, we keep the occurrence distribution for each c_n, as the example shown in Figures 5b and 5c. This distribution enables one not only to know the mean and median fitting values but also to estimate the error range. For example, in the

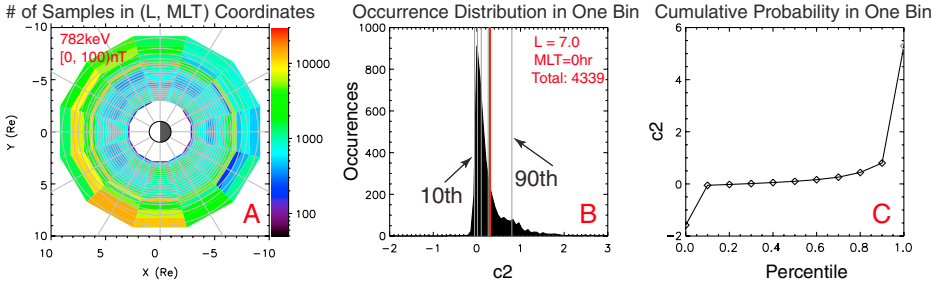

Figure 5. Model grids used in REPAD. (a) Contours of L shell grids (gray circles) and MLT grids (radial gray lines) in the magnetic equatorial plane, which are overplotted on the distribution of data sample numbers for 782 keV electrons within the *AE* range of [0, 100) nT. (b) Occurrence distribution of the normalized fitting coefficient c_2 in one bin (L = 7.0, MLT = 0) selected from Figure 5a. The vertical gray lines indicate c_2 values at five accumulative percentiles from the tenth to ninetieth with an increment of 20, and the red vertical line indicates the mean c_2. (c) Values of c_2 versus occurrence percentiles for the same model bin.

Table 1. Summary of Grid Points in REPAD

	Values
L shell grid points (total number 22)	3.0, 3.2, 3.4, 3.6, 3.8, 4.0, 4.2, 4.4, 4.6, 4.8, 5.0, 5.25, 5.5, 5.75, 6.0, 6.25, 6.5, 6.75, 7.0, 7.25, 8.0, 9.0
Magnetic local time grid points (in hour, total number 12)	00, 02, 04, 06, 08, 10, 12, 14, 16, 18, 20, 22
Energy grid points (in keV, total number 8)	148; 272; 509; 782; 1,090; 1,368; 1,472; 1,582
Three *AE* categories (in nT)	[0, 100); [100, 300); [300, 20,000]
Occurrence percentiles for c_n's (total number 11)	0th, 10th , 20th , …, 90th, 100th

specific bin as shown in Figure 5c, the median c_2 has the value of ~0.1 at the 50th percentile, and the variation ranges between ~ 0.0 and 0.9 from the 10th to the 90th percentiles. This model requests the minimum sample number of 100 in each grid bin to keep the distribution statistically meaningful. A summary of grid points for REPAD is presented in Table 1.

Finally, since coefficients c_n are treated as separate parameters in the model, the independence between each other as well as to the average flux level C_0 need to be confirmed. According to the statistics theory, two events *X* and *Y* are independent if and only if their joint probability, i.e., Prob(*X*, *Y*), equals the product of their individual probabilities, i.e., Prob(*X*) * Prob(*Y*). Here we present examples for 782 keV electrons observed during the whole CRRES mission, as shown in Figures 6 and 7. Figures 6 and 7 (left column) show joint probabilities derived directly from observations, and Figures 6 and 7 (right column) show products of two individual probabilities, derived by collapsing 2-D distributions shown in left to each single dimension.

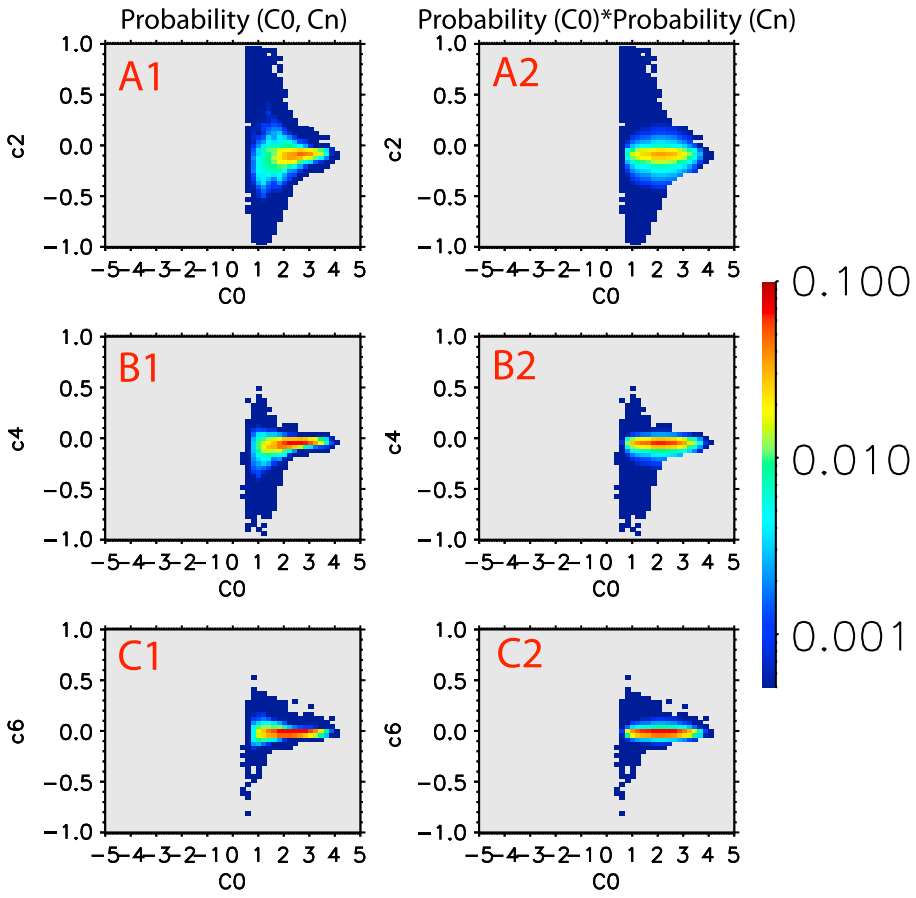

Figure 6. Check the independence between fitting coefficient C_0 and c_n's. (a1) The joint probability distribution of (C_0, c_2), i.e., Prob(C_0, c_2), by fitting PADs for 782 keV electrons as observed during the whole CRRES mission. (a2) The product of two individual probabilities, i.e., Prob(C_0)*Prob(c_2), as calculated from Figure 6a1. (b1, b2) Distributions for C_0 and c_4 in the same format. (c1, c2) Distributions for C_0 and c_6.

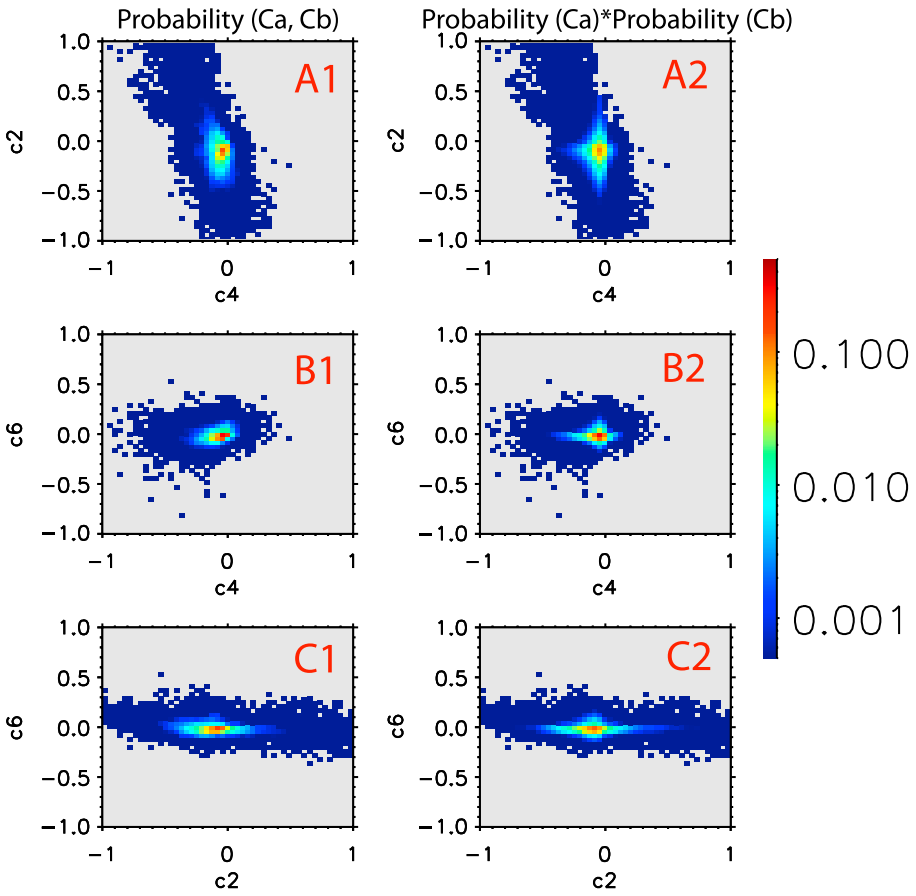

Figure 7. Check the independence between c_n's. The same format as in Figure 6.

Comparing two distributions in each row, one can easily see their similarities. Results for other energies have similar results (not shown here). Therefore, we claim that the usage of c_n as independent model parameters is justified.

4. Model Results and Discussions

This section illustrates distributions from REPAD, though it is difficult to present many details due to the multiple model dimensions. Here we select and present some typical and representative examples, and more can be found in the supporting information. In addition, we also have some initial discussions on possible reasons leading to observed PADs, such as variations for different *AE* categories, but pursuing definitive conclusions will need further detailed studies and thus are left to the future as a separate topic.

First, we present global distributions for the median values of fitting coefficients c_n, which determine PAD shapes and are the most widely used. Figure 8 shows examples for electrons with a moderate energy of 782 keV. One significant feature in these distributions is the difference between two distinct regions separated by L shell at ~6.5. Comparing panels for the two *AE* categories, one can clearly see large variations of c_n in the region outside of L ~6.5 while not much inside. (The inner most region with $L < 4$ also show variations that will be discussed later.) Similar two separated regions are also seen for low- and high-energy electrons (see Figure S2 in the supporting information). This should indicate that electrons in the two regions experience different level of adiabatic effects, which is at least partially related to *AE*, and/or other different physical processes, e.g., magnetopause may indeed reach $L \sim 6.5$ quite often but rarely inward.

For moderate-energy electrons, Figure 8 also shows that the relatively stable PADs in the inside region always stay close to isotropic since all c_n values are very close to zero, while PADs in the outside region are very different and are strongly asymmetric between the dayside and nightside. The same can be read from curves

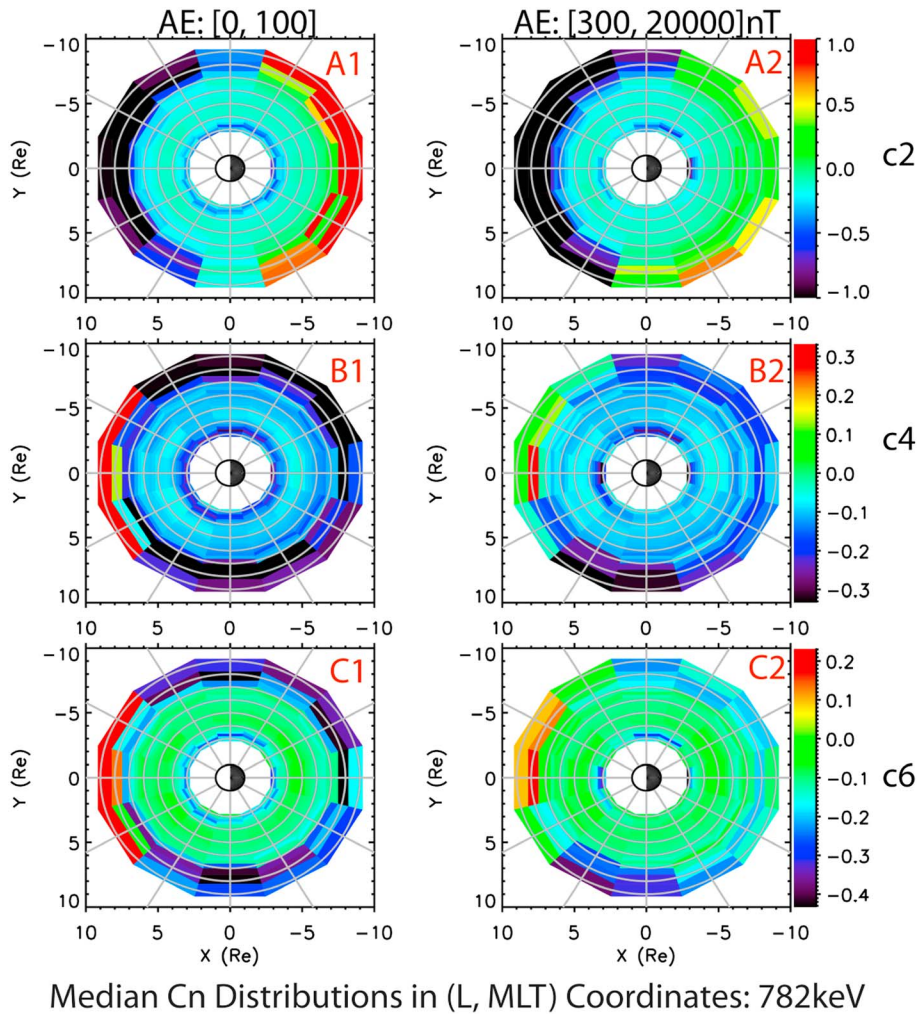

Figure 8. REPAD distributions of median c_n in the magnetic equatorial plane. (a1) Distribution of median c_2 as a function of L and MLT for 782 keV electrons within the lowest *AE* range of [0, 100) nT. (a2) Distribution of median c_2 in the same format for the highest *AE* range of [300, 20,000] nT. (b1, b2) Distributions of c_4 in the same format. (c1, c2) Distributions of c_6.

in Figure 9 (and Figures S3 and S4 in the supporting information). Here we focus on the outside region. During quiet times (i.e., the lowest *AE* category), PADs in dayside are pancake like, by using plots in Figure 4, and those at nightside are butterfly like; while for the highest *AE* category PADs will keep their typical forms but turn to be more isotropic around 90° pitch angle. This asymmetry between day and nightside can be partially explained by drift-shell splitting due to asymmetric magnetic field, while other process (i.e., in situ wave-particle resonance) may also play a role here. PADs for low-energy electrons also turn more isotropic at nightside for high *AE* (Figure S2a), which is consistent with previous results that substorm injected electrons are almost isotropic [*Åsnes et al.*, 2005]. High-energy electrons show similar asymmetry though the dayside pancake PADs turn to be more anisotropic, for which one explanation is due to the steep radial gradient in flux distributions during disturbed periods.

For each bin in the outside region, statistical distributions of c_n exhibit large variations as shown in Figure 9. Another region showing large variation is at L < ~4. Similar variations are seen for high-energy electrons but not for the low-energy electrons (not shown here). This may reflect the resonance effectiveness of hiss waves inside the plasmapause that is much higher with MeV electrons than ~100 keV electrons [e.g., *Meredith et al.*, 2007]. Small variations for the region in between may reflect the dominance of some process with weak pitch angle dependence such as radial diffusion. Focusing on the 00 MLT, as shown in Figure 10, we see that coefficients c_n in the outside region have the tendency to be closer to zero for higher *AE* values, which reflects

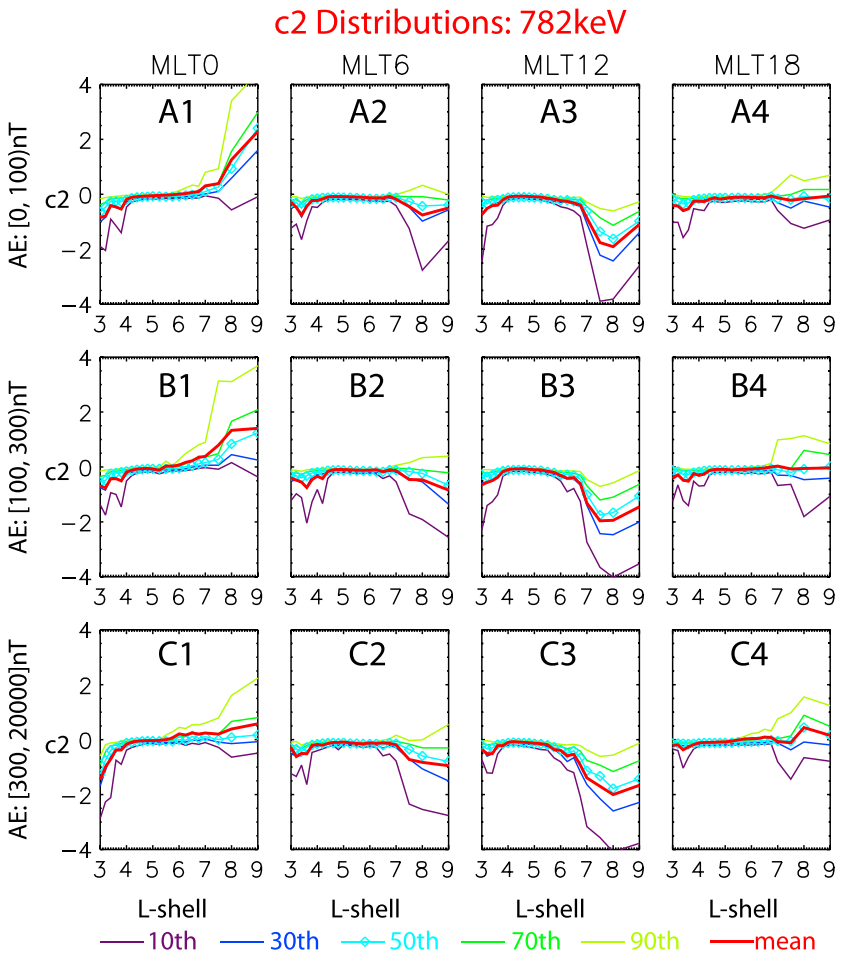

Figure 9. REPAD distributions of c_2 as function of MLT, L, and *AE*. These are for 782 keV electrons. In each panel, c_2 curves are plotted as a function of L shell and color coded for different accumulative percentiles. Curves overplotted with diamond data points (aqua color) are for median c_2 values. (top to bottom) Three rows correspond to three *AE* categories. (left to right) Four columns correspond to four MLTs at midnight, dawn, noon, and dusk, respectively.

some process that works across all pitch angles similarly and thus make PADs more isotropic; while for L < 4, coefficients c_n for moderate- and high-energy electrons turns more negative, which may reflect the hiss wave resonance being stronger for small pitch angles [*Meredith et al.*, 2009]. No matter what is the physics behind, the larger variation in c_n obviously indicates less representative the median/mean PAD distribution and vice versa. Also can be seen from Figure 9 is that the median values (in aqua color) are close to but not overlapping with the mean values (red), indicating occurrence distributions are not normal distributions.

Since REPAD uses three different data sets, it is necessary to check the difference between submodels that are based upon each individual data set. As shown in Figure 11, one can see that submodels agree with each other quite well in most regions, though differences do exist such as at L shells < ~4.5 for moderate-energy electrons (Figure 11, middle row). The differences may come from different instrument performance and/or different mission periods. Since Polar has the largest size of data, REPAD distributions are mostly dominated by Polar observations, except for the GEO region where LANL-97A also has significant numbers of observations.

5. Model Verification and Validation

We verify and validate the model using both in-sample and out-of-sample tests. The in-sample tests can verify that there are no significant algorithm and coding errors in the model development steps. For this purpose, we test the model by comparing individual CRRES, Polar, and LANL-97A data to model fitting results.

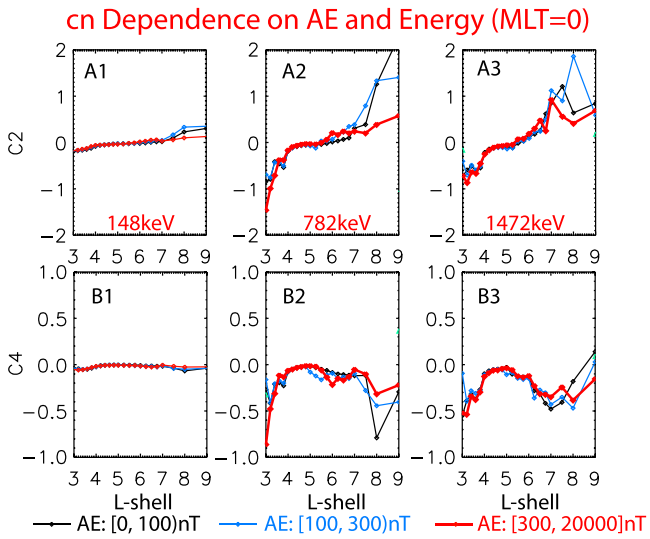

Figure 10. REPAD distributions of c_n as a function of energy, L and *AE*. In each panel, the mean c_n curves at 00 MLT are plotted as a function of L shell and colors indicate different *AE* categories. (top to bottom) Two rows correspond to c_2 and c_4, respectively. (left to right) Three columns correspond to three energies: 148, 782, and 1472 keV, respectively.

From observations shown in Figure 2, for example, we pick fluxes observed at local 90° pitch angles only and feed them to the model, and the fitting results are shown in Figure 12. Figures 12a, 12c, and 12e present fitted fluxes as a function of pitch angle and time, and Figures 12b, 12d, and 12f present the flux ratios between fitted results and observations. Clearly, the model always captures the characteristic shapes of PADs, and fitted fluxes agree with observations fairly well, except for pitch angles close to loss cones at some time. Extra gaps in fitted fluxes come from the L shell limitation of REPAD.

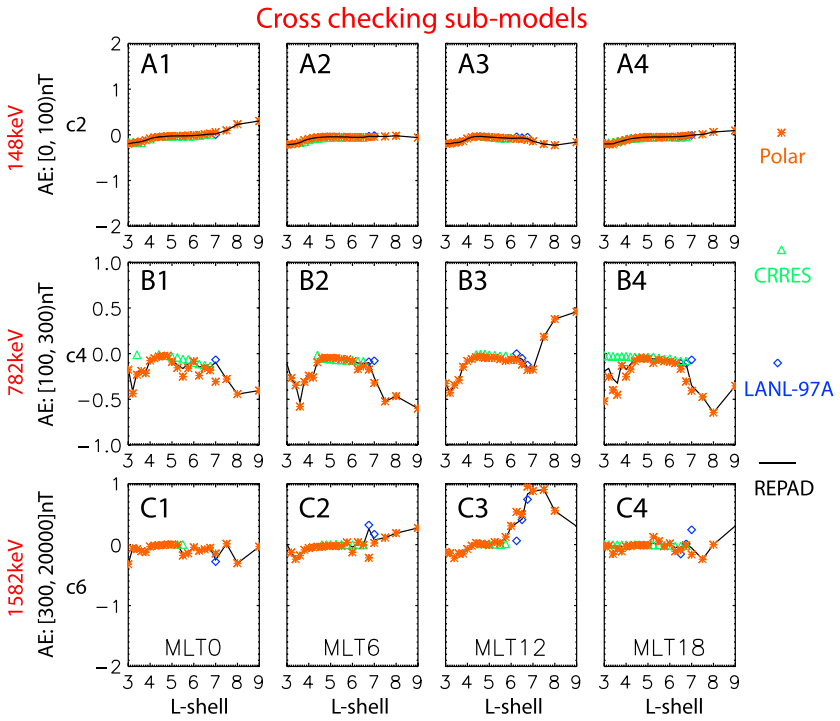

Figure 11. Cross-check fitting coefficients from three submodels. In each panel, c_n is plotted as a function of L and data points with different colors are from different submodels: Orange for Polar, green for CRRES, blue for LANL-97A, and black curves for REPAD. (top to bottom) Three rows are for c_2 for 148 keV electrons in the lowest *AE* category, c_4 for 782 keV electrons in the medium *AE* category, and c_6 for 1582 keV electrons in the highest *AE* category, respectively. (left to right) Four columns are for four MLTs: 00, 06, 12, and 18 MLT.

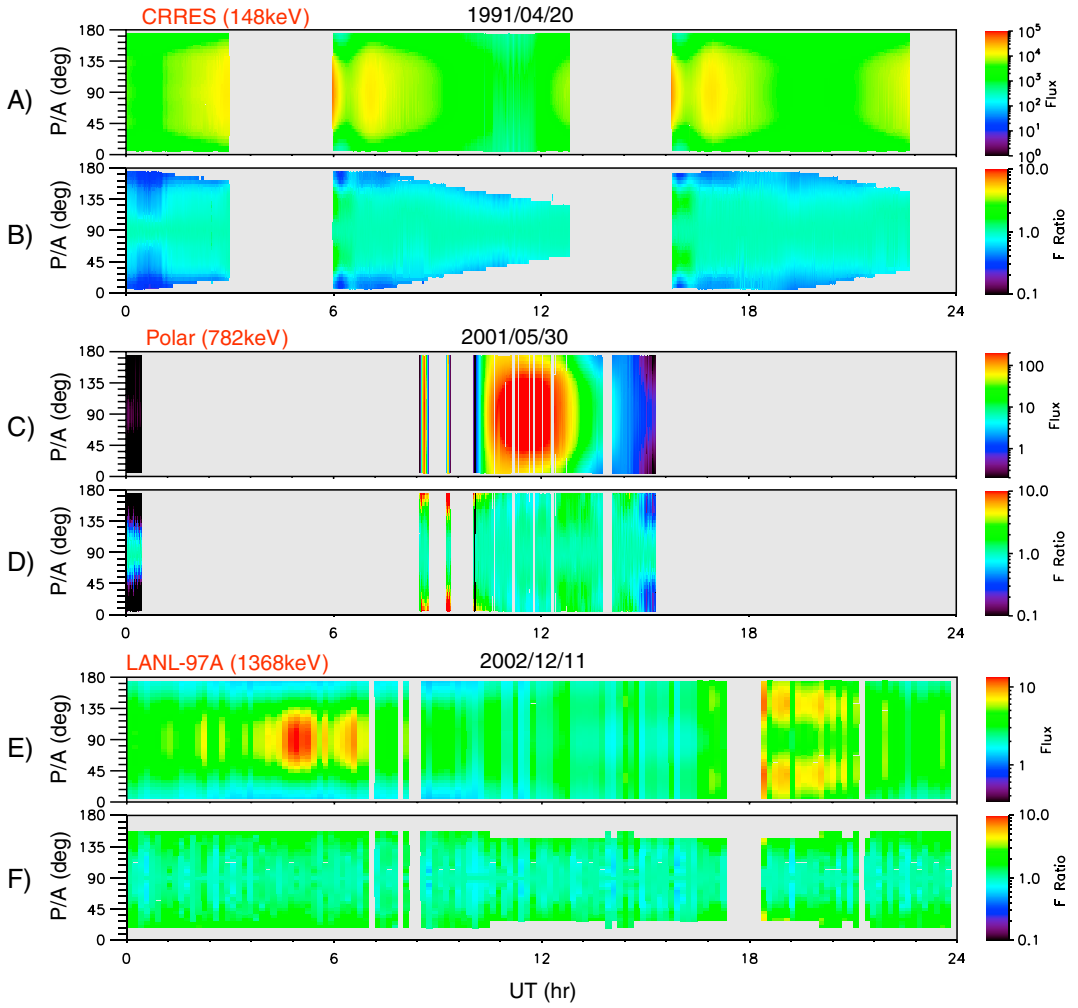

Figure 12. REPAD verification: in-sample tests. (a) Fitted pitch angle resolved fluxes for 148 keV electrons, derived from REPAD using unidirectional fluxes at 90° local pitch angle observed by CRRES on 1 day (20 April 1991). (b) Ratios between fitted fluxes as in Figure 12a and observed fluxes as shown by Figure 2a. (c and d) Fitted fluxes and flux ratios in the same format for Polar on 30 May 2001. Observed fluxes are shown in Figure 2c. (e and f) Fitted fluxes and flux ratios in the same format for LANL-97A on 11 December 2002. Observed fluxes are shown in Figure 2e. Vertical gray gaps in fitted fluxes are either due to original data gaps or L shells being outside of REPAD L range of [3, 9].

For the out-of-sample test, we use the independence data from Van Allen Probes (formerly named RBSP). The two probes a and b have nearly identical, highly elliptical, and low-inclination orbits crossing radiation belt every ~9 h, with the apogee inside of GEO orbit. The Magnetic Electron Ion Spectrometer (MagEIS) instrument on board each measures electrons and ions in the middle energy ranges, and the pitch angle resolved fluxes we have here are from the M75 sensor covering the energy range of ~300–1000 keV [*Blake et al.*, 2013]. Background contaminations on MagEIS from Bremsstrahlung and penetrating protons are not completely removed from data used here, and we assume they have low levels with pitch angle independence and thus have insignificant effects on the measured PADs particularly in the outer belt region. One example is shown for electrons with moderate energy (584 keV) on one magnetically active day, as shown in Figure 13. Again, here we use fluxes at the local 90° pitch angle only as input for REPAD to fit fluxes at other pitch angles. Flux values and ratios shown in Figures 13b and 13c indicate great model performance. Tests on other energies (Figure S5 for low energy and Figure S6 for high energy in the supporting information) for the same day also show similar results. Therefore, this out-of-sample test demonstrates the validity of REPAD.

To systematically evaluate the performance of REPAD, we further use 2 month observations from Van Allen Probes b (October–December 2012) and repeat above steps for each available energy channel. The

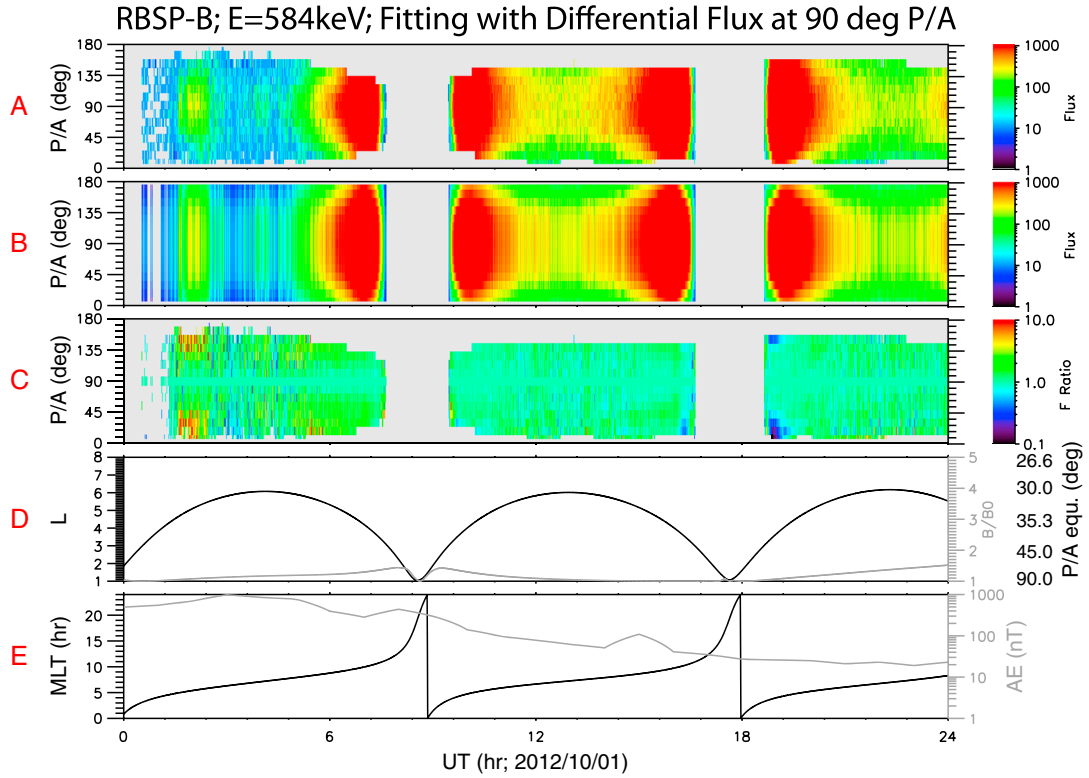

Figure 13. REPAD Validation: Out-of-sample test. (a) Pitch angle resolved fluxes for 584 keV electrons observed by RBSP-b MagEIS instrument on 1 October 2012. Measurements with L < 3 are omitted here due to the L shell coverage of REPAD. (b) Fitted pitch angle resolved fluxes for the same energy, derived from REPAD using unidirectional fluxes at 90° local pitch angle from observations. (c) Ratios between fitted and observed fluxes as in Figures 13b and 13a. (d) Curves for L shell (black) and magnetic field ratio between local and equatorial values (gray). Equatorial pitch angle values (black) corresponding to five magnetic ratios are also given to the right. (e) MLT trace (black) for the satellite and *AE* index (gray).

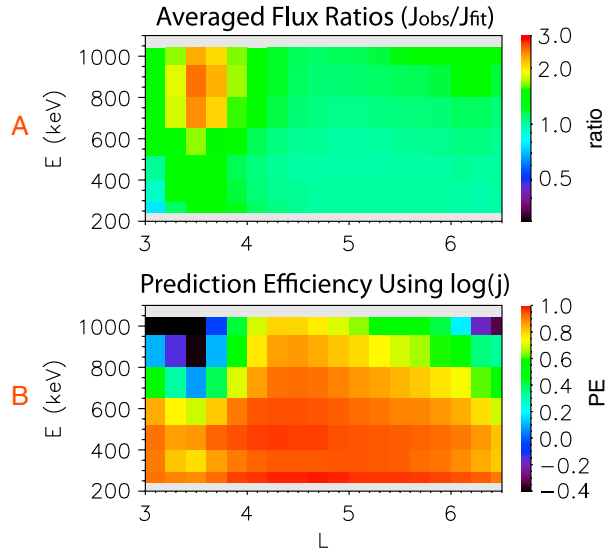

Figure 14. REPAD performance evaluations. By comparing two months Van Allen Probes electron observations to fitted fluxes, we here plot (a) averaged flux ratios and (b) model prediction efficiency on logarithm of fluxes lg(*j*) as a function of L and energy.

model's performance is evaluated in two methods: One is to get the average flux ratios as a function of energy and L shell, as shown in Figure 14a. It can be seen that for most model regions the ratio is close to 1 except for L ~3.5 and energies above 600 keV. This method show how REPAD works in the average sense. The other method is to calculate the performance efficiency (PE) for each model bin so as to evaluate the model's performance from the statistical sense. Here PE in each bin is defined as

$$\mathrm{PE} = 1 - \frac{\Sigma_i \left[\lg\left(j_m^i\right) - \lg\left(j_d^i\right)\right]^2}{\Sigma_i \left[\lg\left(j_d^i\right) - \lg\left(\bar{j}_d\right)\right]^2} \qquad (3)$$

where subscripts *m* and *d* for flux *j* indicate fitted and observed values, respectively, and $\bar{j}_d$ is the mean of observations. Here PE = 1 indicates model results perfectly fit

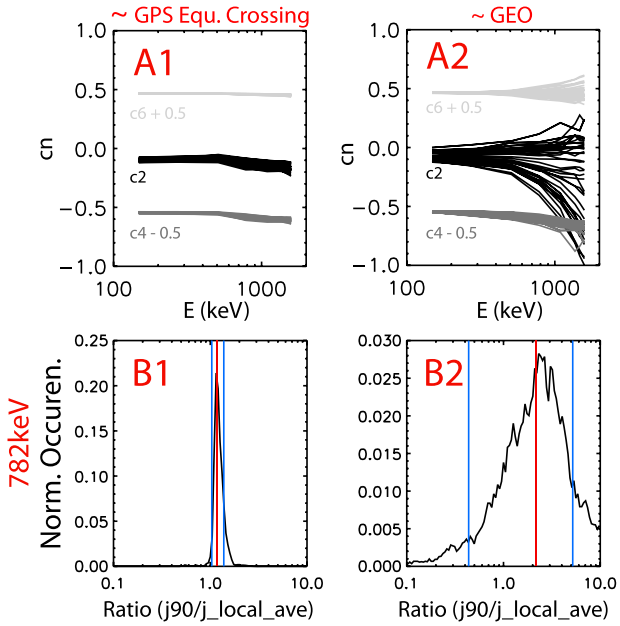

Figure 15. Variations of PADs at two typical L shells. (a1) REPAD fitting coefficients at GPS equatorial crossings with L = 4.2 as a function of energy, compared to (a2) those at ~GEO with L = 6.5. In each panel, black curves are for original median c_2 values for all local times and *AE* categories, dark gray curves are for c_4 downshifted by 0.5 from original values, and light gray curves are for c_6 upshifted by 0.5. (b1, b2) Occurrence distributions of flux ratios for 782 keV electrons observed by CRRES. The ratio is between the flux of equatorially mirroring electrons and locally directionally averaged flux, measured by CRRES but along simulated GPS orbits, at two L shells: ~ GPS equatorial crossings (Figure 15b1) and ~ GEO (Figure 15b2). In each panel, red vertical line indicates the mean ratio, while two blue lines for ratios at the 5th and 95th occurrence percentiles.

observations point to point; PE = 0 means model fit observations with the same average and same variation; and PE < 0 means model may not even fit well to the average of observations. Clearly from Figure 14b, REPAD has PE values equal or larger than 0 in most model domain, particularly for energies lower than 600 keV, except for in the same region with L ~3.5 and energies above 600 keV as in Figure 14a. This region is coincident with the slot region for high-energy electrons (as well as at large L shells), where logarithms of average flux levels (i.e., the C_0) are close to zero, and thus, coefficients c_n as defined in equation (2) may fall close to the singularity point.

6. Application to GPS Data

As mentioned in section 1, one application of REPAD is for GPS electron data. Each GPS satellite has a circular orbit with a radius of 4.2 R_E, inclination of 55°, 12 h period, and crosses the outer electron belt every 6 h at different local times. Since GPS satellites carry only omnidirectional particle sensors, e.g., the Burst Detector Dosimeter IIR [*Cayton et al.*, 1998] onboard ns41, adding pitch angle information to GPS electron observations has significant scientific meaning for radiation belt research.

First, we discuss characteristic electron PADs at two L shells: the GPS equatorial crossing points at L ~ 4.2 and GEO at L ~ 6.5. As pointed out in section 4, at L = 4.2, fitting coefficients c_n are highly stable, showing very small variations and being very close to zero as can be seen from Figure 15a1, while large variations in c_n are seen around the GEO orbit (Figure 15a2). This implies that it is reasonable to assume electrons observed at L = 4.2 have fixed PADs. This is further tested by inspecting into CRRES electron data, which are pitch angle resolved and measured close to the equator. Flying a virtual GPS satellite through the CRRES data set, we are able to simulate its "observed" omnifluxes. Dividing the omnifluxes by 4π, we have the directionally averaged fluxes observed by the virtual satellite. Comparing the directionally averaged fluxes to those measured by CRRES at the same L shell but close to the equatorial plane, we can test the assumption of isotropic PADs. From Figure 15b1, the narrow distribution of flux ratios at L = 4.2 during the whole CRRES mission demonstrates that assuming isotropic PAD will bring an error factor between 1 and 1.5 for 782 keV electrons, while the error factor ranges beyond 0.1–10 for L = 6.5 (~GEO). Similar results are seen for low- and high-energy electrons (Figure S8 in the supporting information). Therefore, the assumption of isotropic PADs works quite well at GPS equatorial crossings, as we did in our previous electron phase space density studies [*Chen et al.*, 2007a], but not so well at GEO orbit.

Bearing in mind that error bars grow at larger L shells, we apply REPAD model to GPS observations throughout the whole outer belt region. Here one example is shown in Figure 16, which is on 1 day with moderate geomagnetic activities. Extrapolation is needed for both L shell (beyond 9) and energy (the highest three energy channels). For each energy channel, given the GPS L shell and MLT at one time point, REPAD provides fitting coefficients c_n that determine the equatorial PAD shape. By finding out the C_0 that can best fit the directionally averaged flux from the observation, we are able to derive the full equatorial pitch angle distribution of fluxes from equations (1) and (2). Knowing the satellite's geomagnetic latitude, we can derive the local pitch angle

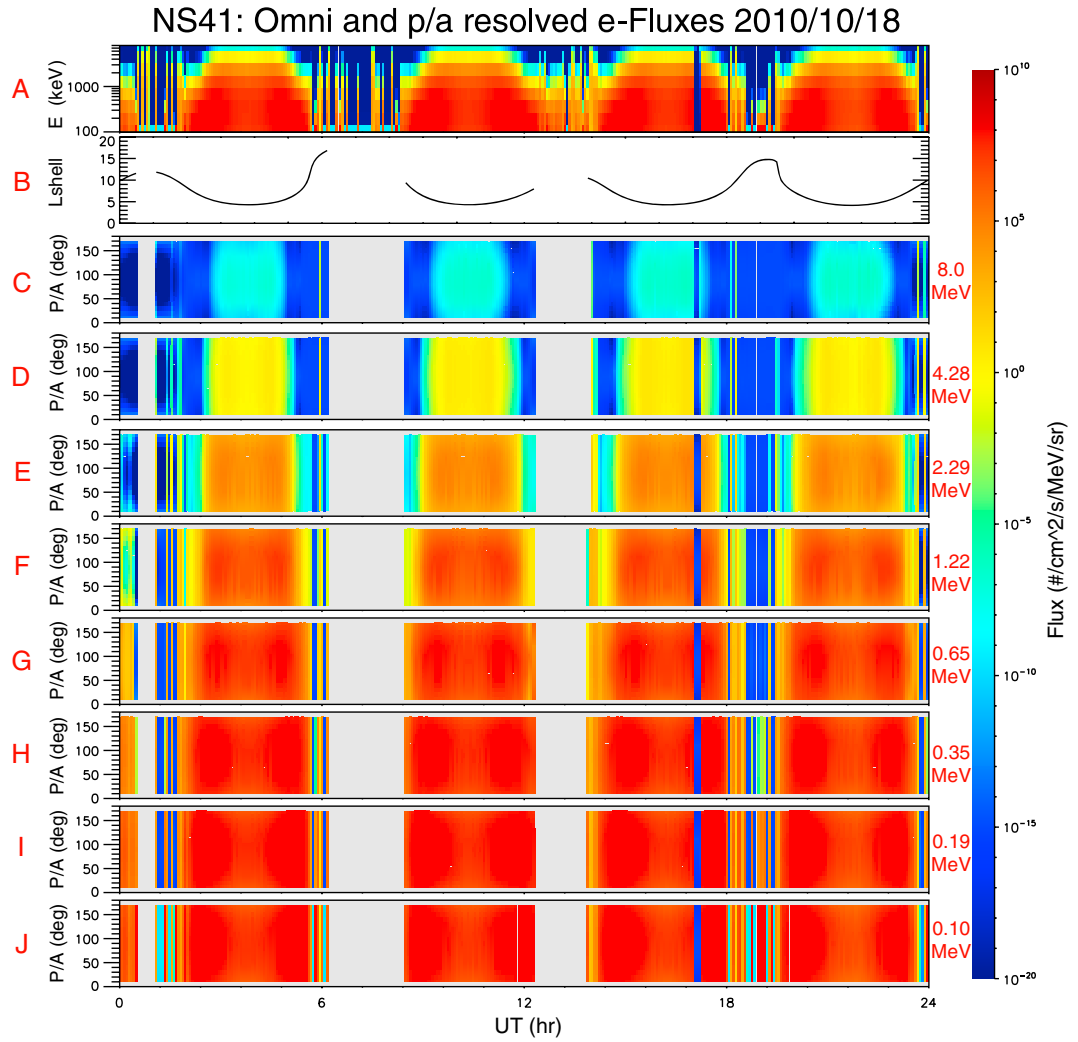

Figure 16. Model application example: Daily GPS fluxes from measurement and pitch angle resolved fluxes fitted using REPAD. (a) Directionally averaged fluxes as a function of energy observed by GPS ns41 on 18 October 2010. (b) L shells of the satellite applying REPAD. (c–j) Fitted local pitch angle resolved fluxes for eight energy channels: 8.0, 4.28, 2.29, 1.22, 0.65, 0.35, 0.19, and 0.10 MeV, respectively.

distribution as shown in Figures 16c–16j. More examples on geomagnetically active and quiet days can be found in Figures S9 and S10 in the supporting information. A processed GPS data set, with fitted pitch angle distribution of fluxes and known error ranges, can be useful for data assimilation models for radiation belts.

7. Summary

We completed a statistical survey on the pitch angle distributions of energetic electron trapped in the Earth's outer radiation belt, and based upon those survey results we developed a new empirical model. This model—REPAD—is able to provide statistical pictures of electron equatorial pitch angle distributions as a function of energy, L shell, magnetic local time, and magnetic activity. To quantify and facilitate this statistical survey, we used Legendre polynomials for fitting long-term in situ directional fluxes observed near the magnetic equator from three missions: CRRES, Polar, and LANL-97A. Covering the whole outer belt region with energies up to 1.6 MeV, REPAD provides not only the mean and median pitch angle distributions but also error bars, which is a new and useful feature that has not existed before. Preliminary verification and validation results demonstrate the model construction, and tests against Van Allen Probes observations validate the model's reliable performance. Usage of REPAD is mainly to predict the full pitch angle distribution of fluxes along a given magnetic field line, or even on a given drift shell, based upon a single-point flux measurement on

that line with limited directional resolution (or not at all). In particular, the very small variations in pitch angle distributions measured with L within ~ 4–5 justify the assumption of fixed pitch angle distributions at GPS equatorial crossings (L ~ 4.2).

Acknowledgments

This work was supported by the AE(P)9 Project funded by NRO, the NSF National Space Weather Program (project 1131871), and the Van Allen Probes, RBSP-ECT funding under NASA's Prime contract NAS5-01072. We want to acknowledge the PIs, instrument teams, and data support teams of CRRES MEA, Polar CEPPAD, LANL GEO SOPA, and Van Allen Probes MagEIS for providing measurements and allowing us to use their data. Special thanks to Tom Cayton and Rod Christensen for preprocessing LANL GEO and GPS data. We are grateful for the use of IRBEM-LIB codes for calculating magnetic coordinates. We also want to thank CDAWeb for providing OMNI data.

Masaki Fujimoto thanks Sebastien Bourdarie and an anonymous reviewer for their assistance in evaluating this paper.

References

Åsnes, A., R. W. Friedel, J. Stadsnes, M. Thomsen, N. Østgaard, and T. Cayton (2005), Statistical pitch angle properties of substorm-injected electron clouds and their relation to dawnside energetic electron precipitation, *J. Geophys. Res.*, *110*, A05207, doi:10.1029/2004JA010838.

Baker, D. N., P. R. Higbie, and E. W. Hones Jr. (1978), High resolution energetic particle measurements at 6.6 R_e. 3. Low-energy electron anisotropies and short term substorm predictions, *J. Geophys. Res.*, *83*, 4863–4868.

Belian, R., G. Gisler, T. Cayton, and R. Christensen (1992), High-Z energetic particles at geosynchronous orbit during the great solar proton event series of October 1989, *J. Geophys. Res.*, *97*, 16,897–16,906.

Blake, J. B., et al. (1995), CEPPAD: Comprehensive energetic particle and pitch angle distribution experiment on POLAR, *Space Sci. Rev.*, *71*, 531–562.

Blake, J. B., et al. (2013), The Magnetic Electron Ion Spectrometer (MagEIS) Instruments Aboard the Radiation Belt Storm Probes (RBSP) Spacecraft, *Space Sci. Rev.*, *179*, 383–421, doi:10.1007/s11214-013-9991-8.

Cayton, T. E., R. D. Belian, S. P. Gary, T. A. Fritz, and D. N. Baker (1989), Energetic electron components at geosynchronous orbit, *Geophys. Res. Lett.*, *16*, 147–150.

Cayton, T. E., D. M. Drake, K. M. Spencer, M. Herrin, T. J. Wehenr, and R. C. Reedy (1998), Description of the BDD-IIR: Electron and proton sensors on the GPS, *Technical Report*, *LA-UR-98-1162*, Los Alamos National Laboratory, Los Alamos, N. M.

Chen, Y., R. H. W. Friedel, G. D. Reeves, T. G. Onsager, and M. F. Thomsen (2005), Multisatellite determination of the relativistic electron phase space density at geosynchronous orbit: Methodology and results during geomagnetically quiet times, *J. Geophys. Res.*, *110*, A10210, doi:10.1029/2004JA010895.

Chen, Y., G. D. Reeves, and R. H. W. Friedel (2007a), The energization of relativistic electrons in the outer Van Allen radiation belt, *Nat. Phys.*, *3*, 614–617, doi:10.1038/nphys655.

Chen, Y., R. H. W. Friedel, G. D. Reeves, T. E. Cayton, and R. Christensen (2007b), Multisatellite determination of the relativistic electron phase space density at geosynchronous orbit: An integrated investigation during geomagnetic storm times, *J. Geophys. Res.*, *112*, A11214, doi:10.1029/2007JA012314.

Friedel, R. H. W., S. Bourdarie, and T. E. Cayton (2005), Intercalibration of magnetospheric energetic electron data, *Space Weather*, *3*, S09B04, doi:10.1029/2005SW000153.

Gannon, J. L., X. Li, and D. Heynderickx (2007), Pitch angle distribution analysis of radiation belt electrons based on Combined Release and Radiation Effects Satellite Medium Electrons A data, *J. Geophys. Res.*, *112*, A05212, doi:10.1029/2005JA011565.

Gu, X., Z. Zhao, B. Ni, Y. Shprits, and C. Zhou (2011), Statistical analysis of pitch angle distribution of radiation belt energetic electrons near the geostationary orbit: CRRES observations, *J. Geophys. Res.*, *116*, A01208, doi:10.1029/2010JA016052.

Higbie, P. R., and W. R. Moomey (1977), Pitch angle measurements from satellites using particle telescopes with multiple view directions, *Nucl. Instrum. Methods*, *14*, 439–445.

Horne, R. B., N. P. Meredith, R. M. Thorne, D. Heynderickx, R. H. A. Iles, and R. R. Anderson (2003), Evolution of energetic electron pitch angle distributions during storm time electron acceleration to megaelectronvolt energies, *J. Geophys. Res.*, *108*(A1), 1016, doi:10.1029/2001JA009165

McIlwain, C. E. (1966), Magnetic coordinates, *Space Sci. Rev.*, *5*, 585–598.

Meredith, N. P., R. B. Horne, S. A. Glauert, and R. R. Anderson (2007), Slot region electron loss timescales due to plasmaspheric hiss and lightning-generated whistlers, *J. Geophys. Res.*, *112*, A08214, doi:10.1029/2007JA012413.

Meredith, N. P., R. B. Horne, S. A. Glauert, D. N. Baker, S. G. Kanekal, and J. M. Albert (2009), Relativistic electron loss timescales in the slot region, *J. Geophys. Res.*, *114*, A03222, doi:10.1029/2008JA013889.

Olson, W., and K. Pfitzer (1977), Magnetospheric magnetic field modeling, *Tech. Rep.*, McDonnell Douglas Astronaut. Co., Huntington Beach, Calif.

Reeves, G. D., K. L. McAdams, R. H. W. Friedel, and T. P. O'Brien (2003), Acceleration and loss of relativistic electrons during geomagnetic storms, *Geophys. Res. Lett.*, *30*(10), 1529, doi:10.1029/2002GL016513.

Roederer, J. (1970), *Dynamics of Geomagnetically Trapped Radiation*, Springer, New York.

Russell, C. T., R. C. Snare, J. D. Means, D. Pierce, D. Dearbourne, M. Larson, G. Barr, and G. Le (1995), The GGS/Polar magnetic field investigation, *Space Sci. Rev.*, *71*, 563–582.

Singer, H. J., W. P. Sullivan, P. Anderson, F. Mozer, P. Harvey, J. Wygant, and W. McNeil (1992), Fluxgate magnetometer instrument on the CRRES, *J. Spacecr. Rockets*, *29*(4), 599–601.

Thomsen, M., D. McComas, G. Reeves, and L. Weiss (1996), An observational test of the Tsyganenko (T89a) model of the magnetospheric field, *J. Geophys. Res.*, *101*, 24,827–24,836.

Vampola, A. L. (1992), CRRES magnetic electron spectrometer AFGL-701-5A (MEA), *J. Spacecr. Rockets*, *29*, 592–596.

Vampola, A. L. (1998), Outer zone energetic electron environment update, in *Conference on the High Energy Radiation Background in Space*, IEEE Proceedings: Conference on the High Energy Radiation Background in Space, Snowmass, Colo., pp. 128–136, IEEE, Snowmass, Colo.

West, H. I., R. M. Buck, and J. R. Walton (1973), Electron pitch angle distributions through the magnetosphere as observed on Ogo5, *J. Geophys. Res.*, *78*, 1064–1081.